Materials Today Chemistry 30 (2023) 101587

Contents lists available at ScienceDirect

Materials Today Chemistry

journal homepage: www.journals.elsevier.com/materials-today-chemistry/

Effect of prelithiation with passivated lithium metal powder on passivation films on high-energy NMC-811 and SiC_x electrodes

E. Esen [a], M. Mohrhardt [a], P. Lennartz [a], I. de Meatza [b], M. Schmuck [c], M. Winter [a, d], E. Paillard [e, *]

[a] Helmholtz-Institute Münster IEK-12, Forschungszentrum Jülich GmbH, Corrensstraße 46, Münster 48149, Germany
[b] CIDETEC Basque Research and Technology Alliance (BRTA), Paseo Miramon 196, Donostia-San Sebastian 20014, Spain
[c] VARTA Innovation GmbH, Stremayrgasse 9, Graz 8010, Austria
[d] MEET – Münster Electrochemical Energy Technology, Corrensstraße 46, Münster 48149, Germany
[e] Politecnico di Milano, Department. of Energy Via Lambruschini 4, Milan 20156, Italy

ARTICLE INFO

Article history:
Received 30 June 2022
Accepted 5 May 2023
Available online 6 June 2023

Keywords:
Li-ion cells
Prelithiation
Passivated lithium metal powder (PLMP)
Stabilized lithium metal powder
Silicon-carbon composite electrode
Active lithium loss
Solid-electrolyte interphase (SEI)
Cathode electrolyte interphase (CEI)

ABSTRACT

The effect of prelithiation using passivated lithium metal powder (PLMP) pressed onto SiC_x anodes is reported for NMC-811|| SiC_x cells with high energy mass loadings. The effect of prelithiation degree and storage time after cell assembly on the formation and growth of the solid electrolyte interphase (SEI) was elucidated by impedance spectroscopy (EIS) and *operando* solid-state ^7Li nuclear magnetic resonance (NMR) spectroscopy, which allowed determining the optimal storage period for the prelithiated cells. The galvanostatic intermittent titration technique (GITT) was used to compare apparent Li^+ diffusion coefficients in prelithiated and non-prelithiated SiC_x electrodes. Furthermore, we show that the electrochemical performance of NMC-811|| SiC_x cells can be dramatically improved by prelithiation using PLMP. In particular, cycle life at 80% state of health (SoH) is almost tripled, increasing from 80 to 228 cycles. Moreover, X-ray photoelectron spectroscopy (XPS) and energy dispersive X-ray (EDX) analysis show that the composition of the cathode electrolyte interphase (CEI) is also markedly modified compared with non-prelithiated reference cells. In particular, the amount of $Li_xPF_yO_z$ species is reduced as prelithiation using PLMP promotes a more effective SEI layer on the SiC_x electrode, richer in LiF and Li_3PO_4, and richer in organic components that probably also contribute to the enhanced cycling stability.

1. Introduction

The performance requirements of lithium-ion batteries have increased proportionally to the increasing demand, especially for those designed for electric vehicles (EVs). As of 2021, the targets for high-performance cells for EV applications were defined as 350 Wh/kg at the cell level and 235 Wh/kg at the pack level (at C/3) by the Department of Energy and the United States Advanced Battery Consortium LLC, with beyond 1000 cycles of operation to a state-of-health (SoH) of 80% [1,2]. Thus, despite the considerable advances in battery research in the last two decades, more research effort is needed to improve the electrochemical performance and cycle life of state-of-the-art (SoA) high gravimetric and volumetric energy density batteries.

Silicon (Si) provides a high theoretical specific capacity of 4200 mAh/g [3] owing to the Si–Li alloying mechanism. Thus, it is a promising candidate for boosting the cell energy density, especially when combined with nickel-rich cathodes, such as lithium nickel-cobalt-aluminum oxide (NCA) with a practical capacity of 180 mAh/g at 4.3 V (vs. Li|Li^+) [1,4] and lithium nickel-manganese-cobalt oxide (NMC-811), with 200 mAh/g at 4.2 V [5]. Despite enabling a high specific capacity, the Si–Li alloying mechanism has a major drawback, as Si particles undergo large volume changes (up to 300%) during lithiation and de-lithiation [6]. Such large volume changes cause Si particles to be pulverized, which eventually causes delamination of the active material [7]. Both pulverization and delamination mechanisms lead to irreversible capacity losses and a fast decay of capacity due to the losses of active material, either as isolated Si particles or delaminated electrode layers [8,9]. Another crucial issue associated with silicon-based electrodes is the continuous consumption of Li^+ ions and other electrolyte species during the (re)formation of the solid electrolyte interphase (SEI)

---

[*] Corresponding author.
E-mail address: elieelisee.paillard@polimi.it (E. Paillard).

https://doi.org/10.1016/j.mtchem.2023.101587
2468-5194/

layer. Besides the loss of Li^+, the continuous thickening of the SEI is another cause of the capacity decay related to internal resistance rise, which also increases self-heating and aging [10]. A common approach to limiting the effects of the volume change of Si particles and the resulting cracking and pulverization is to decrease the Si particle size [11]. However, the resulting increase in surface area goes hand in hand with the consumption of Li and electrolytes. Consequently, much lower initial coulombic efficiency (ICE) values are often reported for Si electrodes (ICE = 25%–75% [11]) compared to state-of-the-art (SOTA) graphite electrodes (ICE > 90%). Several approaches have been proposed for limiting the irreversibility, such as using fluoroethylene carbonate (FEC) as an electrolyte additive [12,13] or preparing silicon carbon (SiC_x) composites mixed with graphite. Unfortunately, such approaches are not sufficient to overcome the limitations of Si-containing electrodes, especially in terms of cycle life.

Prelithiation, on the other hand, is a promising approach for increasing the cycle life by providing a Li reservoir in the cell as well as improving the ICE of Si-containing electrodes. Prelithiation can be performed by short circuiting the anode with a lithium electrode either using a sacrificial lithium electrode in-situ or ex-situ [14], or by using sacrificial Li salts such as 3,4-dihydroxibenzonitrile dilithium salt (Li_2DHBN) [15] or dilithium squarate ($Li_2C_4O_4$) [16], or by direct contact with Li metal foil [17,18] or passivated Li metal powder (PLMP) [19,20] with the negative electrode. Each prelithiation method has its advantages and disadvantages. Prelithiation using sacrificial salts allows precise control of the prelithiation degree and could be compatible with current Li-ion battery production processes, but is made difficult by the volume of undesired gas formation during cell formation cycles [16,21–23].

With PLMP, Wang et al. observed a 10% increase in the delivered discharge capacity after prelithiation of NMC-111 (10.0 mg/cm^2) || graphite (6.0 mg/cm^2) full cells at 0.33C for 50 cycles [24]. Furthermore, Rezqita et al. showed the effect of electrochemical prelithiation for low mass loading electrodes in a NMC 532 (2.85 mg/cm^2) || SiC_x (0.55 mg/cm^2) cell [25]. Forney et al. reported that prelithiation with PLMP dramatically increased the ICE of NCA || Si-carbon nanotube (CNT) full-cells that retained 93% of their initial capacity after 50 cycles at C/5 [11]. Apart from the previously mentioned studies, there is still a gap in the literature about the influence of prelithiation in practical applications utilizing high-energy electrodes with high mass loadings relevant for EV applications. Therefore, we selected SiC_x and NMC-811 electrodes since the desired specific energy (350 Wh/kg) and the energy density (800–1000 Wh/L) for EVs can be achieved with this cell chemistry [1]. Moreover, the direct contact method using PLMP was selected to assess its applicability and challenges. The effect of prelithiation on the performance of NMC-811 (21.0 ± 0.3 mg/cm^2, 4.0 mAh/cm^2) || SiC_x (6.6 mg/cm^2, 4.2 mAh/cm^2) cells is reported here. In particular, we report on the progression of SiC_x lithiation and SEI formation prior to cycling with storage time after cell assembly and its effect on cycling performance, along with the effect of prelithiation using PLMP on passivation films on the SiC_x and NMC-811 electrodes.

2. Experimental methods

2.1. Material preparation

2.1.1. Electrodes used

The cathodes were made using 95% NMC-811 (T81R, Targray) as the active material, 3% polyvinylidene fluoride (PVDF Solef® 5130, Solvay) as the binder, and 2% carbon black (C-NERGY Super C-65, IMERYS) as a conductive additive. Initially, a PVDF solution in N-methyl pyrrolidone (NMP) was prepared. Afterwards, Super C65 and NMC-811 powder were added to the solution under continuous stirring. Finally, the slurry was cast on aluminum foil (Hydro, 20 μm) and NMC-811 electrodes with a mass loading of 21.0 mg/cm^2 (4.0 mAh/cm^2) were prepared. Dried electrodes were then calendered to 3.2 g/cm^3 (thickness: 85 ± 2 μm). The NMC-811 electrodes had a specific capacity of 200 mAh/g_{NMC811} and were dried at 120 °C for 16 h under vacuum before cell assembly.

The negative electrodes contained 94% of a SiC_x composite as the active material, 1% C-65 as a conductive additive, and a mixture of carboxymethyl cellulose (CMC, 2%) and styrene-butadiene rubber (SBR, 3%) as binders. The electrodes were cast on a 10 μm-thick copper foil and calendered to 3.2 g/cm^3. The active mass loading of the SiC_x electrodes was 6.6 mg/cm^2 (4.2 mAh/cm^2). The SiC_x electrodes had a total specific capacity of 636 mAh/g and they were dried at 80 °C for 24 h under vacuum before cell assembly.

2.1.2. Electrolyte preparation

The electrolyte used in this study was composed of 1 M lithium hexafluorophosphate salt ($LiPF_6$, ENCHEM, purity: 99.8%) dissolved in ethylene carbonate (EC, Merck, battery grade), dimethyl carbonate (DMC, BASF, purity: 99%), diethyl carbonate (DEC, Soulbrain, purity: 99.98%), and fluoroethylene carbonate (FEC, Solvay, purity: 99.9%) (wt. 3:3:3:1) solvents with an additive mixture of 2 wt% vinylene carbonate (VC, BASF, battery grade) and 0.5 wt% lithium bis(trifluoromethanesulfonyl)imide (LiTFSI, 3 M, battery grade).

2.1.3. Prelithiation of SiC_x electrodes

The anodes were prelithiated using passivated lithium metal powder (PLMP). The amount of PLMP used was 2.5 wt% with respect to the weight of the NMC-811, corresponding to 48.2% of the NMC-811 capacity. The particle size of PLMP (China Energy Lithium) varied between 20 μm and 50 μm, diameter, with a *ca.* 1 μm-thick Li_2CO_3 passivation layer that was not taken into consideration for the capacity calculation. The PLMP was spread onto electrode surfaces with a spatula and activated by pressing by hand with a mylar foil in an argon-filled glovebox ($H_2O < 0.5$ ppm, $O_2 < 0.5$ ppm).

2.2. Electrochemical investigations

2032 type coin cells were assembled using the SiC_x anodes (dried under vacuum at 60 °C for 24 h, diameter: 13 mm) coupled with NMC-811 positive electrodes (dried under vacuum at 120 °C for 16 h, diameter: 12 mm) in an argon-filled glovebox ($H_2O < 0.5$ ppm, $O_2 < 0.5$ ppm) using microporous Celgard 2500 separators (dried under vacuum at 60 °C for 24 h) wetted with 100 μL of electrolyte. In addition, three-electrode Swagelok™-type were assembled in the glovebox, using Li metal (99.99%, Rockwood lithium) as the reference electrode to observe the evolution of the negative and positive electrode potentials of the reference and prelithiated cells during electrochemical cycling.

A Bio-logic VMP III potentiostat was used for open circuit voltage (OCV) measurements and for electrochemical impedance spectroscopy (EIS) measurements (frequency range: 1 MHz to 0.01 Hz, amplitude: 10 mV) for the reference and prelithiated NMC-811 || SiC_x cells. All EIS measurements were performed under OCV conditions using 2032-type coin cells at 40 °C in a climatic chamber (KB400, Binder GmbH). For all reference cells and the cells with prelithiated anodes, OCV measurements were started right after cell assembly ($t = 0$ h). To allow for temperature stabilization at 40 °C, the impedance measurements were performed an hour after connecting each cell to the VMP setup ($t = 1$ h in the graphs).

Distribution of relaxation times (DRT) analysis with a regularization parameter of 10^{-5} (λ) was done using the RelaxIS software to determine the number of R-CPE elements required to define the equivalent circuit, and the most suitable modified Randles circuit was determined as $Z = R_{bulk} + R_{SEI}\text{-CPE } 1 + R_{ch\text{-}tr}\text{-CPE } 2 + W$

(diffusion), with R: resistance elements, CPE: constant phase elements, and W: Warburg element [26]. Impedance data were fitted with the equivalent circuit using RelaxIS software. Areal normalization was done by multiplication of the impedance data with the area of the electrodes (unit: Ω/cm^2).

Galvanostatic cycling of NMC-811$\|$ SiC_x cells was carried out on a MACCOR series 4000 battery cycler in 2032-type coin cells with a Celgard 2500 separator. The cells were placed in a climatic chamber (KB400, Binder GmbH) at 20 °C. The cut-off voltages were 2.8 V and 4.2 V. Formation consisted of one cycle at C/10, followed by three cycles at C/3. Afterwards, the cells were cycled at 1C with a constant current, constant voltage charging step (CCCV, 1C, 0.05C), and a cycle at C/10 was performed every 20 cycles to investigate the capacity retention of the cells at low current.

The galvanostatic intermittent titration technique (GITT) was used to investigate the effect of prelithiation on Li^+ ion diffusion kinetics of the SiC_x electrodes. The method is based on applying pulses of $\tau = 10$ min, at C/10, until the cell is charged. Each pulse was followed by a 20 h rest period. The potential of the positive and negative electrodes was measured *vs.* a Li metal reference electrode using three-electrode Swagelok™ cells. For this measurement, the temperature was kept at 20 °C and the prelithiation degree was set to 2.5 wt%. The apparent diffusion coefficients of Li^+ in SiC_x electrodes were calculated for the reference and prelithiated cells using equation (1) [4] and confirmed using equation (2) [27]. In equation (1), m_B stands for the mass of active material in the electrode, while M_B, V_M, A, and τ stand for the molar mass of SiC_x (92% Gr & 8% Si), molar volume (M_B/ρ) of SiC_x, electroactive surface area of the electrode (⌀ = 12 mm), and pulse time, respectively. It should be noted that electroactive surface area was calculated by excluding the active carbon (1 wt% C-65) and binder (5 wt% CMC-SBR) ratios in the electrode. ΔE_s and ΔE_τ are the differences between the end of the pulse potential and the equilibrium potentials before the next pulse, respectively. In the second equation, I is the applied pulse current, F is the Faraday constant (96485 s A/mol), and Z_A is the charge number of the ionic species, which is '1' for the Li^+ ion, respectively.

$$D_{Li^+} = \frac{4}{\pi.\tau}\left[\frac{m_B.V_M}{M_B.A}\right]^2\left[\frac{\Delta E_s}{\Delta E_\tau}\right]^2 \tag{1}$$

$$D_{Li^+} = \frac{4}{\pi}\left[\frac{I.V_M}{Z_A.F.A}\right]^2\left[\frac{\Delta E_s}{\Delta E_\tau}\right]^2 \tag{2}$$

2.3. Nuclear magnetic resonance spectroscopy

Li insertion into the SiC_x electrode was followed by *in-situ* solid-state ^{7}Li nuclear magnetic resonance (NMR) spectroscopy for 3 weeks after prelithiation of the electrode. The symmetrical pouch cells (2 cm × 6 cm) were assembled in a glovebox ($H_2O < 0.5$ ppm, $O_2 < 0.5$ ppm) without the positive electrode (NMC-811) and separator and only contained two prelithiated (2.5 wt% Li) SiC_x electrodes (12⌀ mm). The PLMP powder was placed on the anodes and activated by applying pressure ot the electrodes inside a glovebox. The prelithiated cell was wetted with 40 μl electrolyte before sealing the pouch cell. The measurements were performed using a Bruker Avance III spectrometer equipped with a widebore magnet operating at 200 MHz (4.7 T). A home-built, broadband probe with a double-resonance Helmholtz-type coil was used for the static ^{7}Li NMR measurements. All spectra were referenced to the ^{7}Li resonance of an aqueous 1 M LiCl solution (set to 0 ppm) and were recorded at a ^{7}Li Lamour frequency of 77.8 MHz. The recycle delay (d1) was alternated between 0.5 s and 4 s, and 512 scans were averaged for each spectrum. The first measurement was conducted 15 min after cell assembly, and the following measurements were conducted every hour for the first 12 h (20 °C). Afterwards, the cell was placed at 40 °C, and measurements were repeated once every day for the following 11 days until the Li metal peak disappeared. In addition, two NMR measurements were conducted after 2 and 3 weeks of storage at 40 °C. All measurements were conducted at room temperature (23 °C). Since the spin-lattice relaxation time T1 for lithiated silicon is around 0.2 s and that of lithium intercalated into graphite is between 1 and 4 s, two measurements were conducted at each measurement time by varying recycle delays (d1) of 0.5 s and 4 s in order to distinguish between the overlapping lithiated graphite (Gr) and lithiated Si peaks so that the differences between the spectra allow obtaining information about the lithiated phases.

2.4. Scanning electron microscopy

An Auriga field emission scanning electron microscope (FE-SEM) with a Schottky field emission gun (Carl Zeiss) was used to investigate the surface morphology of the pristine SiC_x and NMC-811 electrodes as well as the cycled electrodes in reference and prelithiated cells. All cycled cells were disassembled in a glovebox ($H_2O < 0.5$ ppm, $O_2 < 0.5$ ppm). The cycled electrodes were washed three times with 100 μL DMC and transferred to the SEM chamber in a vacuum-sealed sample holder to avoid exposure to air. An in-lens secondary electron detector was used to obtain all images at an accelerating voltage of 3 kV (working distance: 3 mm). The elemental distribution of the electrode surfaces was analyzed after 300 cycles at 1C rate by energy-dispersive X-ray spectroscopy (EDX) using an X-Max 80 mm^2 detector (Oxford Instruments) at a 20 kV operating voltage. The NMC-811 and SiC_x electrodes cycled in the prelithiated and reference cells were retracted from the cells in a glovebox ($H_2O < 0.5$ ppm, $O_2 < 0.5$ ppm) and rinsed using diethylene carbonate (DEC) to remove the salt impurities. Afterwards, all electrodes were dried under vacuum prior to measurement and placed in a vacuum-sealed, airtight sample holder for transfer to the device.

2.5. X-ray photoelectron spectroscopy

X-ray photoelectron spectroscopy (XPS) measurements were performed for non-prelithiated and prelithiated SiC_x electrodes after 300 cycles in order to understand the influence of the prelithiation on the SEI and CEI compositions. The cells were disassembled in an argon-filled glovebox ($H_2O < 0.5$ ppm, $O_2 < 0.5$ ppm) and the electrodes were washed 3 times with 100 μL DMC and completely dried before they were attached to the XPS sample holder using a double-sided conductive carbon tape. The samples were transferred to the XPS device (Thermo VG Scientific, type K-Alpha; calibrated on copper, silver, and gold reference samples) in an air-tight sample holder to avoid exposure to air. All measurements were conducted the same day to limit the aging of the samples. The XPS measurements were performed using a monochromatic Al Kα source, and the pass-energies of the survey spectra and high-resolution core spectra were 200 eV and 30 eV, respectively. The charging of samples was compensated by a charge neutralizer. The XPS data fitting was carried out using CasaXPS software, and the F 1s peak (685.0 eV) was taken as the internal reference for spectra adjustment.

3. Results and discussion

3.1. Impedance evolution upon prelithiation

EIS measurements were performed on the prelithiated NMC-811 $\|$ SiC_x coin cells (2.5 wt% Li) to investigate the SEI growth over a 4-wees storage period at 40 °C. The impedance spectra of the prelithiated cell are compared to a reference cell in Fig. 1a. As can be seen, for the reference cell, only minimal changes in impedance were observed in 4 weeks. On the contrary, significant changes are seen in the prelithiated cell. According to the equivalent circuit shown in the inset, Fig. 1b shows the evolution of the bulk resistance (R_{bulk}), SEI resistance (R_{SEI}), and charge-transfer resistance ($R_{ch\text{-}tr}$) for the prelithiated (2.5 wt% Li) cell and that of the reference cells at $t = 1$ h and $t = 4$ weeks. It can be seen from Fig. 1b that the total cell resistance ($R_{total} = R_{bulk} + R_{SEI} + R_{ch\text{-}tr}$) of the prelithiated cell increases with storage time.

Bulk resistance is the smallest contributor to the total impedance. It slightly increases for 2 weeks and stays constant for the rest of the rest period. As reported by Choi et al., R_{bulk} does not change much with the state-of-charge (SoC), and it gives information on the state-of-health (SoH) of the cells since it is mainly affected by electrolyte depletion over cycling, micro-crack formation in particles, binder decomposition, gas evolution, and current collector dissolution in the cells [28]. Hence, the slight increment in R_{bulk} can be attributed to micro-crack formation as a result of Li insertion in SiC_x electrodes as well as electrolyte consumption due to SEI formation reactions that occur after cell assembly [29]. The first semi-circle in the middle frequency region (from 15 Hz to 10 kHz) corresponds to R_{SEI} and increases for both reference and prelithiated cells over 4 weeks of storage, whereas the second semi-circle at lower frequencies (in the 0.1 Hz−300 Hz region) typically corresponds to $R_{ch\text{-}tr}$ [30] and does not change much as compared to the SEI resistance upon storage. The change in R_{SEI} in the non-prelithiated cell can be explained by the reaction of $LiPF_6$ with protic impurities such as water or hydrolytic electrolyte decomposition due to hydroxyl (-OH) and carboxylic acid (-COOH) substituents on the CMC binder and carbon present in the negative electrode [31]. However, the change in R_{SEI} is much smaller in the reference cell since reactions contributing to passivation films prior to cycling are limited compared to the prelithiated cell. R_{SEI} increases for the prelithiated cell during the first 7 h after cell assembly and stays constant for 2 days before starting to increase again. The change in the SEI and the consequent total resistance became more dramatic after one week of storage at 40 °C indicating that the SEI film gets continuously thicker and more resistive after assembly. The SEI film is a normally dynamic interphase that gets thicker and thinner as the electrode potential varies [32] with an overall increase over cycling. Here, since the prelithiated cell is not cycled, the SEI thickness continuously increases with storage time. Besides the thickness, the composition of the SEI also affects the R_{SEI}. Thus, the analysis of SEI components was done using XPS and EDX and is presented in the following.

3.1.1. NMR analysis of the prelithiated SiC_x electrode

The effect of storage after cell assembly was investigated by *in-situ* solid-state ^{7}Li nuclear magnetic resonance (NMR) spectroscopy for the prelithiated SiC_x electrode. Due to the Knight shift, lithium metal and lithium ions are well separated in ^{7}Li NMR spectra. Changes in the lithium metal peak (~245−275 ppm) and changes in the electrolyte and SEI peaks (−10 to 10 ppm) were observed along with the formation of the lithiated Gr and Si−Li alloy peaks (−40−45 ppm) [33]. Neither the Li metal peak nor the electrolyte peak changed during the first 12 h after pressing the PLMP onto the electrodes and electrolyte addition (Fig. S3). As can be seen from Fig. 2a, the Li metal peak begins to gradually diminish 24 h after the cell assembly as a result of Li insertion in the SiC_x electrode and the SEI formation reactions onto Li. Shellikeri et al. reported, by visual observations, that their Li powder completely disappears in 24 h after applying it to the anodes when soaked into the electrolyte [34]. However, Fig. 2a shows that the Li metal peak is only halved after 4 days of storage and that it took more than 7 days for all Li metal to completely disappear from the electrode surface. As reported by Bärmann et al. for similar Si/Gr electrodes prelithiated using PLMP, Li insertion into the electrode, the reaction of PLMP with the electrolyte and Li de-insertion from the electrode to contribute to the SEI formation compete on the wetted surface of the electrode after electrolyte contact [35]. However, it took longer for these competing reactions to proceed compared to what had been reported insofar in the literature for the prelithiated electrodes, likely due to differences such as electrode properties and electrolyte amount [34,35].

The peaks related to the lithiation of the prelithiated SiC_x electrode were first observed 2 days after cell assembly (Fig. 2b) and distinguished via the use of two different recycle times (d1). The outer lines correspond to both Si−Li and Gr-Li phases, whereas the inner lines of each spectrum correspond to the Si−Li phases, as shown in more detail in Fig. S4. According to the NMR spectra, both Si-site and Gr-site lithiation started 2 days after the cell assembly, whereas a more visible difference could be observed after 6 days of storage. This agrees with the decrease of the Li metal peak during the first 6 days of storage after cell assembly. The formation of LiC_{36} and $Li_{15}Si_4$ results in chemical shifts between 0 and 5 ppm, while LiC_{27}, LiC_{18}, and $Li_{13}Si_4$ give peaks between 5 and 10 ppm [35]. Considering the overlap and the possible formation of small deceptive peaks due to fitting, assigning each lithiation stage would

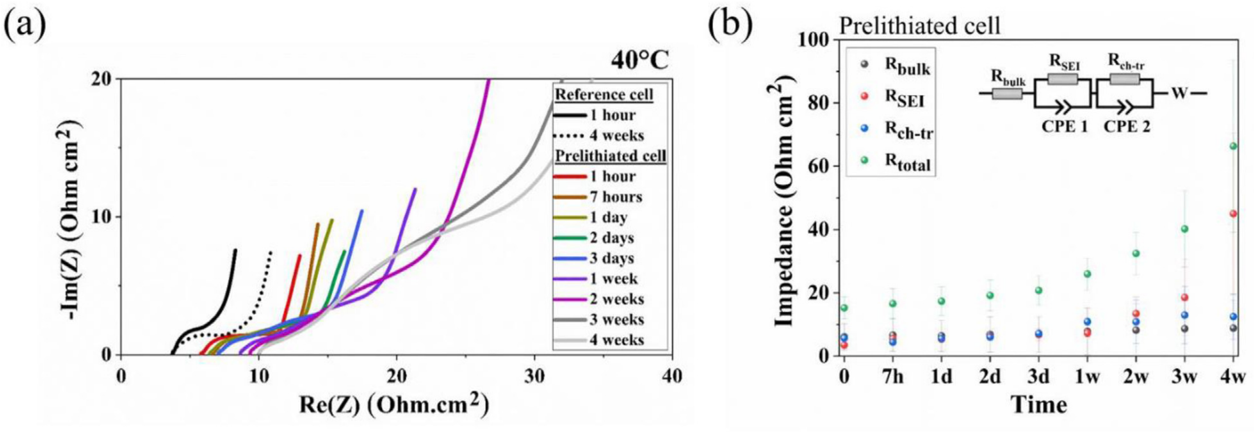

Fig. 1. (a) Nyquist plots of prelithiated (2.5 wt% Li) and reference NMC-811||SiC_x cells at 40 °C. (b) Change of R_{bulk}, R_{SEI} and $R_{ch\text{-}tr}$ for the prelithiated cell (2.5 wt%Li).

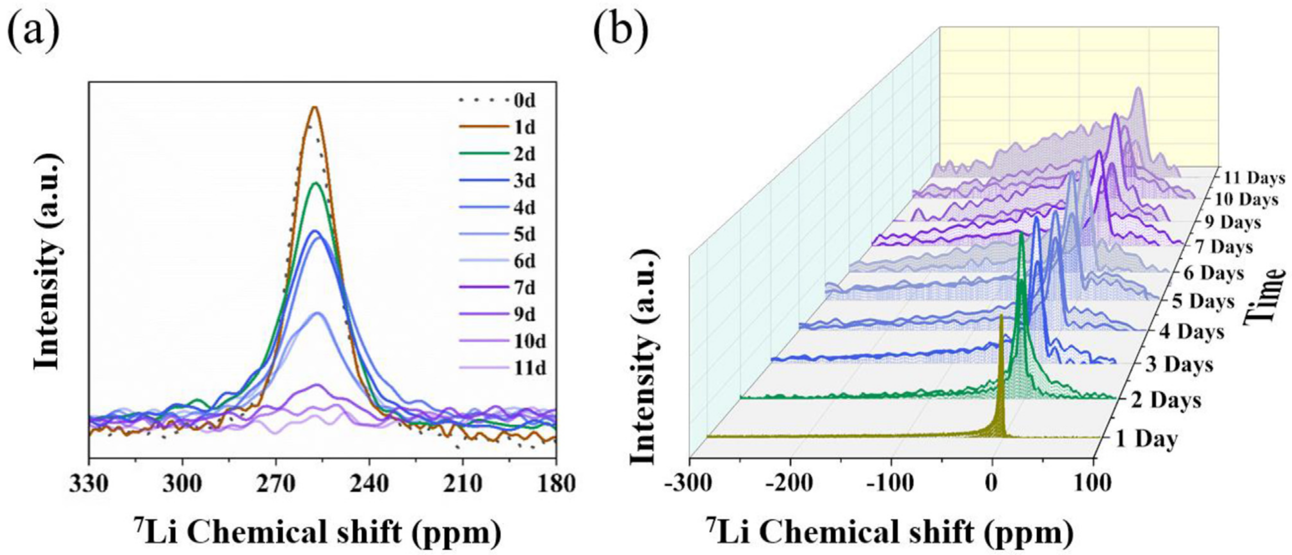

Fig. 2. Evolution of ^{7}Li NMR spectra of prelithiated (2.5 wt% Li) SiC_x electrodes with storage time (a) Evolution of the Li metal peak (b) Evolution of the Li ions peaks. The two NMR spectra shown for each rest time are obtained with d1 = 0.5 s (inner lines) and d1 = 4s (outer lines) recycle delays. Arbitrary Y-axis was normalized separately for the Li metal peak (a) and the Li ions peak (b) for easier observation. ($T_{storage}$: 40 °C, $T_{measurement}$: 23 °C).

not be an appropriate way to evaluate these data. However, Li_7Si_3 (15–20 ppm), $Li_{12}Si_7$ (~20 ppm), LiC_6 (~40 ppm), LiC_{12} (~45 ppm), and $Li_{15+a}Si_4$ (~-10 ppm) have more distinguishable chemical shifts [35] that show that fully lithiated phases coexist with partially lithiated phases within the SiC_x electrode. It can also be seen from Fig. 2b that the Li ion peak (−10 to 10 ppm) gradually gets wider during the 7 days of storage after cell assembly due to continuous consumption of electrolyte and growth of the SEI. This is in agreement with the SEI resistance evolution shown in the previous section. However, following the evolution of the SEI after 10 days of storage was not feasible since the peak related to the electrolyte was masked by the growing $LiPF_6$ peak (−200 to 50 ppm) as electrolyte was continuously consumed throughout the storage period. To sum up, the PLMP was completely consumed by lithiation of the SiC_x electrode and SEI formation reactions approximately 9 days after cell assembly. The further SEI growth is likely due to Li deinsertion as the electrolyte reacts with the lithiated electrode (Fig. S2) during the prolonged storage period. The effects of storage time on cycling performance will be discussed further in the following.

3.2. Li^+ ion diffusion kinetics in prelithiated and unlithiated SiC_x electrodes

Li^+ diffusion during the first lithiation of SiC_x electrodes (charge of the cell up to 4.2 V) were analyzed by the galvanostatic intermittent titration technique (GITT) using a three-electrode cell consisting of a SiC_x anode, an NMC-811 cathode, and a Li reference electrode, used to monitor the potential of each electrode during cycling. The apparent Li^+ diffusion coefficients were calculated using equations (1) and (2). The changes of the apparent Li^+ diffusion coefficients of the reference and prelithiated SiC_x electrodes with their potential vs. Li/Li^+ are shown in Fig. 3a and b, respectively. The electrode potentials where lithiation of graphite occurs are marked with green Roman numbers, and the regions where pronounced Si–Li alloying is expected are marked with blue asterisks. The calculated Li^+ diffusion coefficients were 2–3 times lower for the prelithiated SiC_x electrode compared to that of the reference SiC_x electrode, resulting from overall slower kinetics linked to previous insertion and phase changes (trapped Li^+, grain boundaries) as well as more extensive SEI growth. The relative change of coefficients with regard to the electrode potential, on the other hand, showed a similar trend for the reference and prelithiated cells. The initial plateau ($E_{negative}$ < 0.25 V vs. Li/Li^+, D_{Li^+} ~ 2 × 10^{-13} m^2/s) corresponds to the most ‘dilute stage’ of lithiation of graphite (Li_xC_6, $0 < x < 0.22$), where Si–Li alloying is low [36] and is not discussed here. Three peaks (I, II, and III) corresponding to different graphite stages are observed for both cells with onset potentials ($E_{negative}$) of 0.192 V, 0.102 V, and 0.063 V (vs. Li/Li^+) as reported in Fig. S7 for the reference cell. Despite being slightly lower, these values are in agreement with what was reported by Yao et al. for Si-Gr electrodes [36]. A considerable acceleration in Li^+ diffusion is observed when the potential decreases to 0.192 V (cell voltage: 3.702 V, Fig. 4), as LiC_{30} begins to form at the ‘I’ mark [36]. Furthermore, after this first peak, a continuous increment in the Li^+ diffusivity is observed starting from $E_{negative}$ < 0.18 V vs. Li/Li^+ due to more Si–Li alloying ($E_{negative}$ < 0.18 V vs. Li/Li^+) [37], which culminates with a small peak at 0.126 V (vs. Li/Li^+). At approximately 0.11 V (vs. Li/Li^+), in addition to ongoing Si–Li alloying, LiC_{12} is formed by further lithiation of LiC_{18} [36,37], resulting in a dramatic increase in Li^+ diffusivity.

Region III marks the beginning of the phase change from LiC_{12} to LiC_6; however, the upper cell cut-off voltage of 4.2 V was reached by the reference cell when the negative electrode potential had only decreased to 0.081 V (vs. Li/Li^+). Thus, complete lithiation of graphite (LiC_6) and formation of crystalline $Li_{15}Si_4$, expected below 0.06 V ($E_{negative}$, vs. Li/Li^+), were not observed for the reference SiC_x electrode [36,37]. Unlike the reference cell, the prelithiated electrode reached 0.044 V (vs. Li/Li^+) at the end of the charge step, and Fig. 3b shows the formation of LiC_6 from LiC_{12} at around 0.075 V (vs. Li/Li^+) at the ‘III’ mark. An increase in coefficients is then seen starting from 0.06 V ($E_{negative}$ vs. Li/Li^+) corresponding to the formation of crystalline $Li_{15}Si_4$. Thus, we can conclude that fully lithiated phases form in the prelithiated SiC_x electrode. The calculated apparent Li^+ diffusion coefficients ranged between 7.61 × 10^{-14} m^2/s ($E_{negative}$: 0.78 V vs. Li/Li^+) and 1.74 × 10^{-11} m^2/s

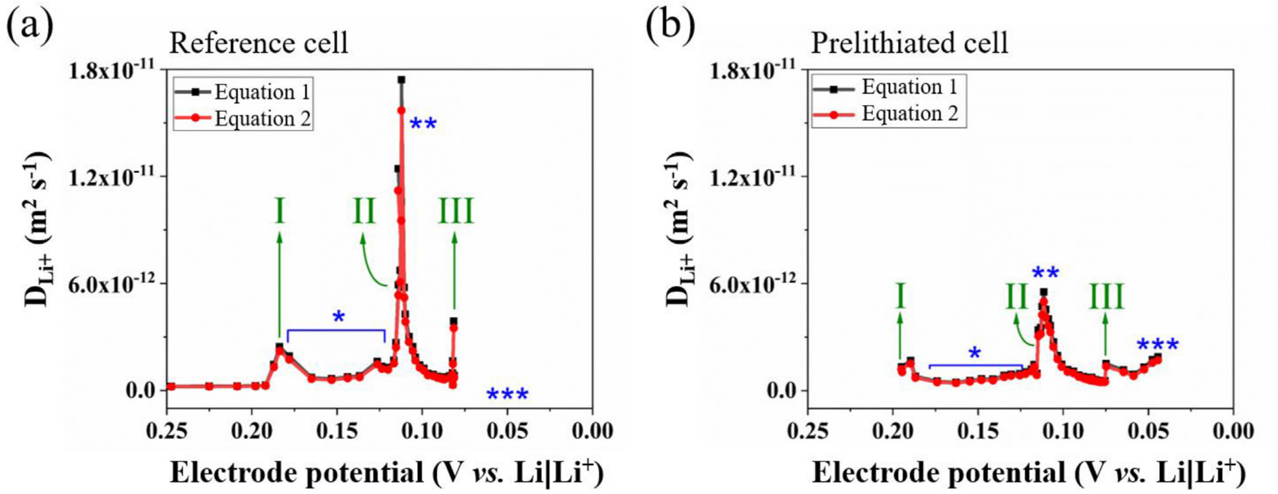

Fig. 3. Change of apparent Li^+ diffusion coefficients in SiC_x composite electrodes as a function of the anode potential during the first lithiation (a) Reference NMC-811||SiC_x cell, (b) NMC-811||SiC_x cell with prelithiated (2.5 wt% Li) SiC_x electrode ($T_{measurement}$: 20 °C).

($E_{negative}$: 0.11 V vs. Li/Li^+) for the SiC_x electrode in the reference cell, which is coherent with the values reported in the literature for graphite and Si-containing electrodes [38,39].

3.3. Cycling performance

The voltage profiles of NMC-811 || SiC_x cells, including a Li metal reference electrode to monitor the potential of each electrode and kept at rest for 7 days after cell assembly, are shown in Fig. 4a and b for a reference and a prelithiated cell, respectively, along with the corresponding potential profiles of each electrode.

As can be seen, in the first charge at C/10, the potential of the prelithiated anode starts at ca. 0.5 V. The end-of-charge potential of the prelithiated anode is lower at 0.002 V vs. Li/Li^+. It indicates that the effective prelithiation level was not high enough to compensate for the capacity difference between anode and cathode and the irreversibility in the first cycle and did not induce lithium plating at C/10. During the first discharge, however, the anode stays more lithiated, with a markedly lower potential at the end of discharge (and correspondingly a lower end of discharge potential for the cathode). The end of charge potential of the prelithiated SiC_x electrode decreased below 0 V (vs. Li|Li^+) after the constant current (CC) charge step during the second formation cycle (at 0.33 C), which also happened in the fifth cycle for the reference SiC_x electrode when the C-rate was increased to 1 C. Since the reference electrode senses the potential in between the anode and the cathode in the T-cell, it is likely that an uncompensated ohmic drop explains this, as the potential then reaches values above 0 V during the constant voltage step as the ohmic drop decreases. It is, however, possible that plating occurs to some degree and then participates in lithiating the anode during the CV step. Over cycling at 1C (Fig. 4c and d), one can see that the evolution of the potentials is different, with the end of discharge potential of the non-prelithiated anode starting at 0.80 V and stabilizing toward 1.23 V after ca. 300 h (i.e. corresponding to full delithiation). In contrast, the prelithiated anode end of the discharge potential starts at 0.56 V and reaches only 0.87 after 600 h. This is a priori very favorable for limiting both the loss of active material in the anode since Si volume changes are then less marked upon cycling, which limits the pulverization phenomenon as well as the loss of lithium inventory due to the SEI formation. The loss of lithium inventory can be well seen with the fast reduction of the potential range of the cathode in the reference cell. Fig. 4e compares the voltage profiles of the two cells and highlights that, due to prelithiation, the initial capacity is increased and the capacity fading is less pronounced.

Fig. 5a and b compare the capacity retention over cycling of NMC-811||SiC_x coin cells with the same prelithiation degree (2.5 wt % Li vs. NMC-811) cycled at 20 °C after different rest periods ranging from 7 h to 4 weeks at 40 °C and a reference non-prelithiated cell, and Table 1 lists their ICEs, highest specific discharge capacities at 1C, and their cycle life at 80% SoH.

As can be seen, the rest time after cell assembly strongly affects the electrochemical performance of the prelithiated cells in terms of ICEs, irreversible capacity loss, and delivered discharge capacity. Starting the cycling after 7 h seems to be advantageous in terms of ICE with 83.8%. vs. 79.9% for the reference cell. Nevertheless, the cycle life is then similar to the reference, with 82 cycles to reach 80% SoH. With longer rest times, the capacity retentions improve markedly up to one week (Fig. 5a). The cycle life of the cells rested for 1 and 3 days increased by 31% and 68%, respectively. The most remarkable improvement is observed for the cell rested for 7 days, with a cycle life almost tripled (228 cycles). For these cells, lower capacities during the initial 30 cycles at 1C rate can be attributed to the higher resistances (as seen in Fig. 1b) compared to the reference cell, causing a lower rate capability. Besides these initial cycles, the capacity is superior compared to the reference cell throughout 300 cycles for all cells with rest times between 1 day and 7 days. Since prelithiation increases cell resistance prior to cycling, its effects on internal resistance change throughout long-term cycling were also investigated via the difference between the average charge and discharge voltages (ΔV) [40] that is plotted in Fig. 5c and d. The increase in total cell resistance after the formation cycles is higher for all prelithiated cells compared to the reference cell. This can be attributed to R_{bulk} and R_{SEI} values that were already higher for the prelithiated cells compared to the reference cell prior to cycling. Despite the initially higher increment in the cell resistance, ΔV reached values similar to those of the reference cell after 300 cycles for prelithiated cells that were kept at rest for 7 days or shorter periods (Fig. 5c). Thus, we can conclude that impedance rise due to electrolyte depletion and electrode degradation over cycling is moderated in the prelithiated cells since the anode was cycled over a narrower potential range (especially towards delithiation, where the volume changes are the highest), which resulted in a slower rise of impedance over long-term cycling. In terms of capacity at C/10,

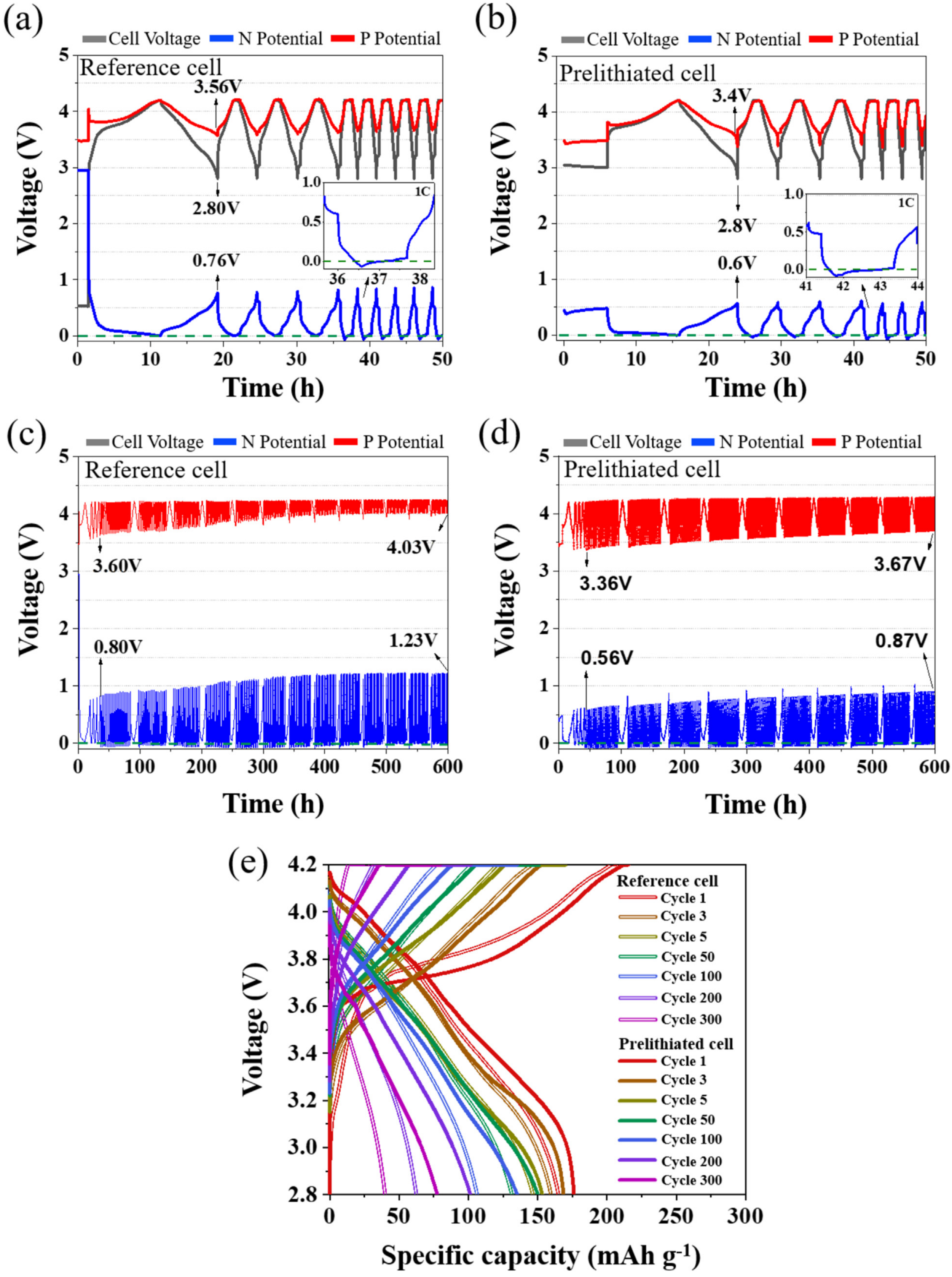

Fig. 4. Evolution of cell voltage and electrode potentials over cycling (CCCV charge and CV discharge) in (a, c) Reference NMC-811‖SiC_x cell and (b, d) Cells with prelithiated SiC_x electrode ((a) and (b) show the first few cycles while (c) and (d) show the potential change over 300 cycles), (e) Voltage profiles of the reference (double line) and prelithiated (single line) cells. Prelithiation degree: 2.5 wt% Li, Three-electrode cell setup with Li reference electrode ($T_{cycling}$: 20 °C, 1 formation cycle at 0.1C followed by 3 formation cycles at 0.33C and 300 cycles at 1C (1C = 200 mA/$g_{NMC-811}$)).

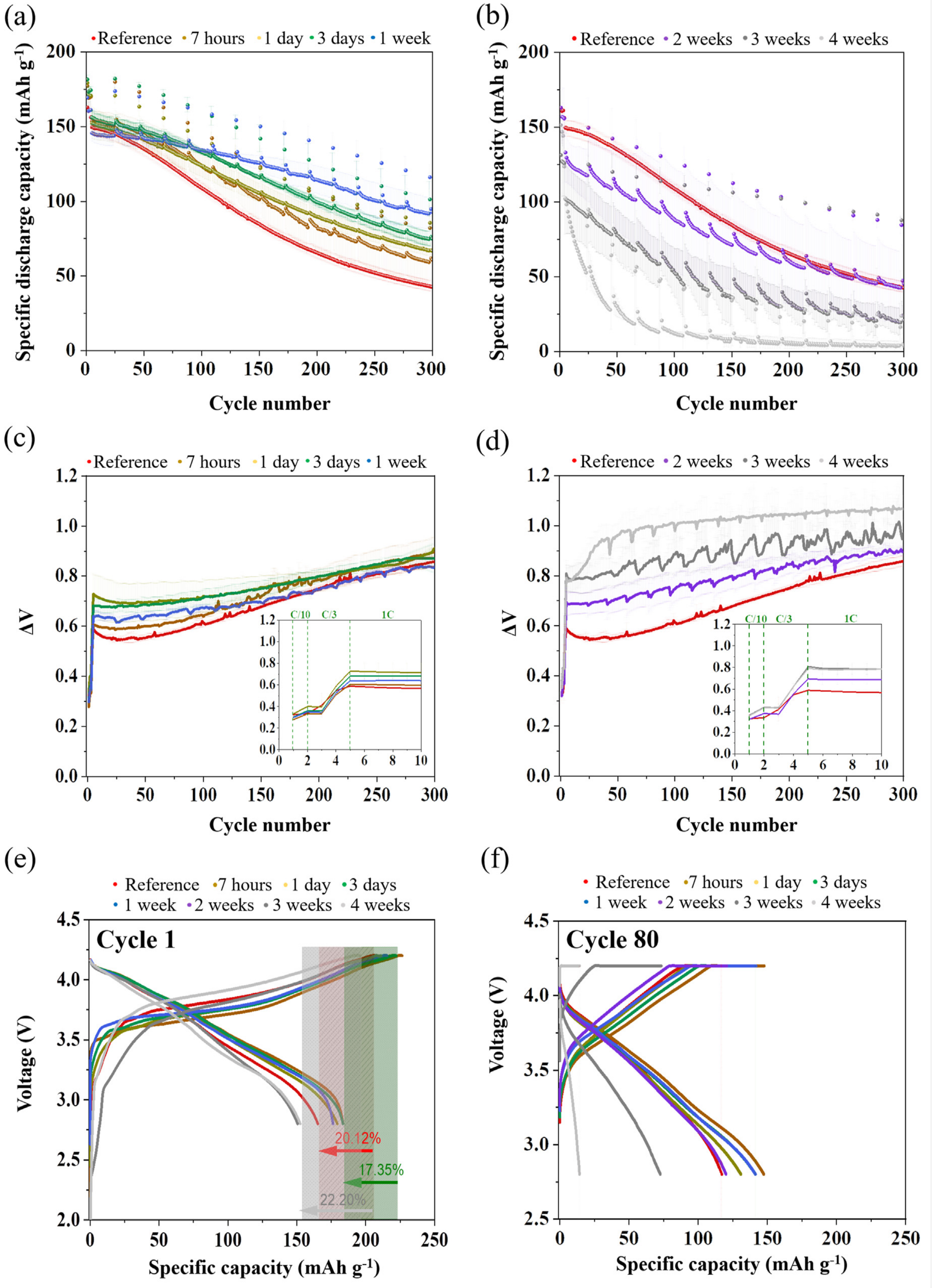

Fig. 5. Specific discharge capacity of reference and prelithiated cells stored for (a) 7 h – 1 week and (b) 1–4 weeks prior to cycling. Difference between average charge and discharge cell voltages (ΔV) of reference and prelithiated cells stored for (c) 7 h – 1 week and (d) 1–4 weeks prior to cycling. (e) 1st cycle voltage profiles, and (f) voltage profile at 80th cycle of reference and prelithiated cells cycled after various storage times. (Prelithiation degree: 2.5 wt% Li, storage time of reference cell prior to cycling: 1 week, $T_{storage}$: 40 °C, $T_{cycling}$: 20 °C).

Above one week rest time, time the capacity retention decreases considerably as seen in Fig. 5b. The ICE values, cumulated Coulomb inefficiencies of the formation cycles (Irr (1–4)) (Table 1) also dramatically deteriorated with the rest time for rest times l longer than 1 week. The ΔV evolution over 300 cycles (Fig. 5d) shows that, not only were the cell

76.5% of the initial discharge capacity was retained after 297 cycles by the cell that was rested for one week.

3.4. Post-mortem analysis

3.4.1. SEM/EDX analysis

The surface morphology changes of SiC_x and NMC-811 electrodes after 300 cycles were investigated by scanning electron microscopy (SEM) (Fig. 6), to observe the influence of the prelithiation on the SEI and the CEI development. Clear evolutions were observed for both non-prelithiated SiC_x (Fig. 6c) and prelithiated SiC_x (Fig. 6e) electrodes after 300 cycles: The pristine SiC_x electrode is mainly composed of flake-like graphite particles with sharp edges and smaller composite SiC_x particles. After 300 cycles, the amount of graphite particles on the surface is strongly reduced, and the surface is composed mainly of whitish particles for both reference and prelithiated SiC_x electrodes, a likely result of the expansion and covering by SEI film of the SiC_x particles. Additionally, it can be seen from Fig. 6a, c, and d that the SiC_x surface in both the reference and prelithiated cells becomes rougher over cycling. As shown by Benning et al. using AFM, the surface roughness of SiC_x particles was tripled following the SEI formation during the first lithiation [41]. They have shown that the SEI formation starts around individual particle clusters at the initial stage of cycling, and reduction products of Li salts and of the solvent begin to fill between the particles, ending up forming a thick layer covering the top of the electrode surface, which increases the surface roughness as cycling proceeds [41]. A lower interstitial porosity due to SEI accumulation is observed for the prelithiated electrode (Fig. 6e) indicating that the growth of SiC_x particles was more pronounced compared to that of the non-prelithiated SiC_x electrode (Fig. 6c). Thicker SEI around the larger aggregates of SiC_x can be expected to act as a buffer for overall volume changes for the prelithiated electrode. Considering the SEM images and results of the galvanostatic charge discharge tests (Fig. 5), where improvement of the cycling stability was obvious for the prelithiated cells, it can be concluded that prelithiation affects the SEI and consequently the cycling performance. The SEI composition and how it is affected by prelithiation will be further discussed in the next sections via EDX and XPS analysis.

Moreover, the surface morphology of NMC-811 particles from both types of cells is also compared. Fig. 6b shows the pristine NMC-811 electrode, and the enlarged (25kx) inset shows the surface of secondary NMC811 particles with interstices between primary particles well visible. After 300 cycles, a layer of passivation film (CEI) is seen on the NMC-811 particles, either cycled in a reference cell (Fig. 6d) or paired with a prelithiated anode (Fig. 6f). The CEI appears much thinner for the prelithiated cell, as the particle boundaries are still well visible, whereas for the reference cell, the CEI layer is thicker and covers the boundaries between primary particles. The differences in surface morphology of the cycled NMC-811 electrodes are likely to be caused by possible cross-talk (material migration) between the positive and negative electrodes and/or the higher average potential seen by the electrodes over cycling.

The EDX results are shown in Fig. 7 for a pristine SiC_x electrode and after 300 cycles for both a reference electrode and a prelithiated one (2.5 wt% Li). Homogeneously distributed sodium, coming from the sodium carboxymethyl cellulose (CMC) binder, was excluded in the figures for easier visualization of the outer surface composition. As can be seen from Fig. 7a, on the surface of the pristine electrode, carbon occupies most of the surface, and some domains are much richer in Si and poorer in carbon. After 300 cycles for both the reference electrode (Fig. 7b) and the prelithiated electrode (Fig. 7c), the proportion of area with visible Si is much higher, which confirms that the Si–C (or Si) particles have expanded as a result of the repetitive volume changes upon cycling. The possible contributions of the electrolyte components to the inorganic and organic layers of the solid electrolyte interphase (SEI) are given in Fig. 7 on the negative electrode in the reference cell [42–44]. [42–44]. The surface passivation films are dominated by phosphorus (P) and fluoride (F) elements for both electrodes after 300 cycles. The source of phosphorus is the conductive salt $LiPF_6$ in the electrolyte, which produces LiF and $Li_xPO_yF_z$ as reduction products [45,46]. The distribution of P and F atoms on the reference SiC_x electrode (Fig. 7b) indicates the presence of a $LiPF_6$-derived ($Li_xPO_yF_z$–based) passivation film on the negative electrode after 300 cycles, especially on the Si-rich surfaces [47]. For the prelithiated SiC_x electrode, phosphorus products seem to be distributed homogeneously on the surface, showing that $LiPF_6$ contributes to passivation of the negative electrode; however, the intensity of phosphorus in the surface film is much lower compared to that of the SiC_x electrode in the reference cell.

A considerable increase in the F element was observed on the surface of the prelithiated SiC_x electrode after 300 cycles. Besides $LiPF_6$ [43,44], LiTFSI [43], and FEC [44,48] are potential fluorine sources in the electrolyte formulation used that can form LiF as a reduction product. In addition to reduction products such as Li_xCF_y, $Li_2SO_2CF_3$ [49] and LiTFSI (1 wt% in the electrolyte used) is expected to form Li_xS, Li_xSyO_z, and LiF upon reduction, which would contribute to the inorganic part of the solid-electrolyte interphase [43]. However, sulfur was not detected; thus, it can be said that the contribution of LiTFSI to the inorganic part of the SEI was not prominent besides the formed LiF. Furthermore, Okuno et al. used density functional theory (DFT)-based molecular dynamics (MD) and the blue-moon ensemble technique to show that formation of LiF requires almost no activation energy if Li^+ ions were present nearby when FEC was in the reduced state [13] and Takenaka et al. showed by hybrid Monte Carlo (MC)/molecular dynamics (MD) reaction simulations that, on carbon-based electrodes, the amount of LiF generated in the presence of the $PF6^-$ anion was small compared to the amount of LiF produced by the FEC additive [50]. Furthermore, it was shown by Okuno et al. that lithium atoms in the lithiated Si bond with the F in the LiF aggregate, which acts as a glue for the organic SEI film components and improves the stability of the passivation film on the negative electrode [13]. A robust SEI is necessary to limit continuous electrolyte and cyclable Li consumption in the cells in order to prevent, or at least limit-the capacity decay upon cycling. Despite the fact that LiF is known to be a resistive and insoluble component in SEI, its effectiveness with a Si-containing electrode has been shown by multiple studies [13,51]. To understand why, we must consider that the prelithiated electrode stays for one week at a relatively low potential (i.e. below 0.5 V vs. Li/Li$^+$) without reaching a potential as low as that reached during cycling. Thus, results in more extensive reactivity of FEC into LiF and organic compounds as the potential is not low enough to achieve full SEI formation (which would be even more protective). This is coherent with the EIS and cycling results that show an increase in impedance with rest time and an optimum reached at one week of

---

impedances much higher during the formation cycle, but also reached a much higher value after 300 cycles. Thus it can be concluded that, rest time between cell assembly and cycling is crucial for the prelithiated cells and it should be optimized before operation to obtain maximum performance in terms of ICE, delivered specific discharge capacity and cycle life. It is likely that resting the cells for too long induces increased reactions with the electrolyte as the anode is maintained as a low potential for a longer time, without -for most electrode parts-ever reaching a potential low enough for reaching a more complete SEI formation, which induces continuous SEI growth and is detrimental to cell performance in terms of impedance growth and loss of lithium inventory.

Table 1
Initial Coulomb efficiency (ICE), cumulated Coulomb inefficiencies between cycle 1 and 5, and cycle life (80% SoH) information of reference and prelithiated (2.5 wt% Li) NMC-811|| SiC_x cells cycled after different storage time at 40 °C.

	Reference	7 Hours	1 Day	3 Days	1 Week	2 Weeks	3 Weeks	4 Weeks
ICE	79.9%	83.8%	82.9%	82.6%	81.4%	81.6%	78.4%	77.8%
Irr (1−4)	26.2%	23.0%	25.4%	23.3%	25.5%	25.9%	30.5%	56.6%
Irr (1−5)	34.9%	34.9%	36.4%	32.0%	36.0%	37.6%	47.4%	62.95%
Max. specific discharge capacity at 1C (mAh/g)	146.8	146.6	152.4	152.9	152.2	148.4	118.9	108.6
Cycle life (80% SoH)	Cycle 80	Cycle 82	Cycle 105	Cycle 134	Cycle 228	Cycle 48	Cycle 39	Cycle 11

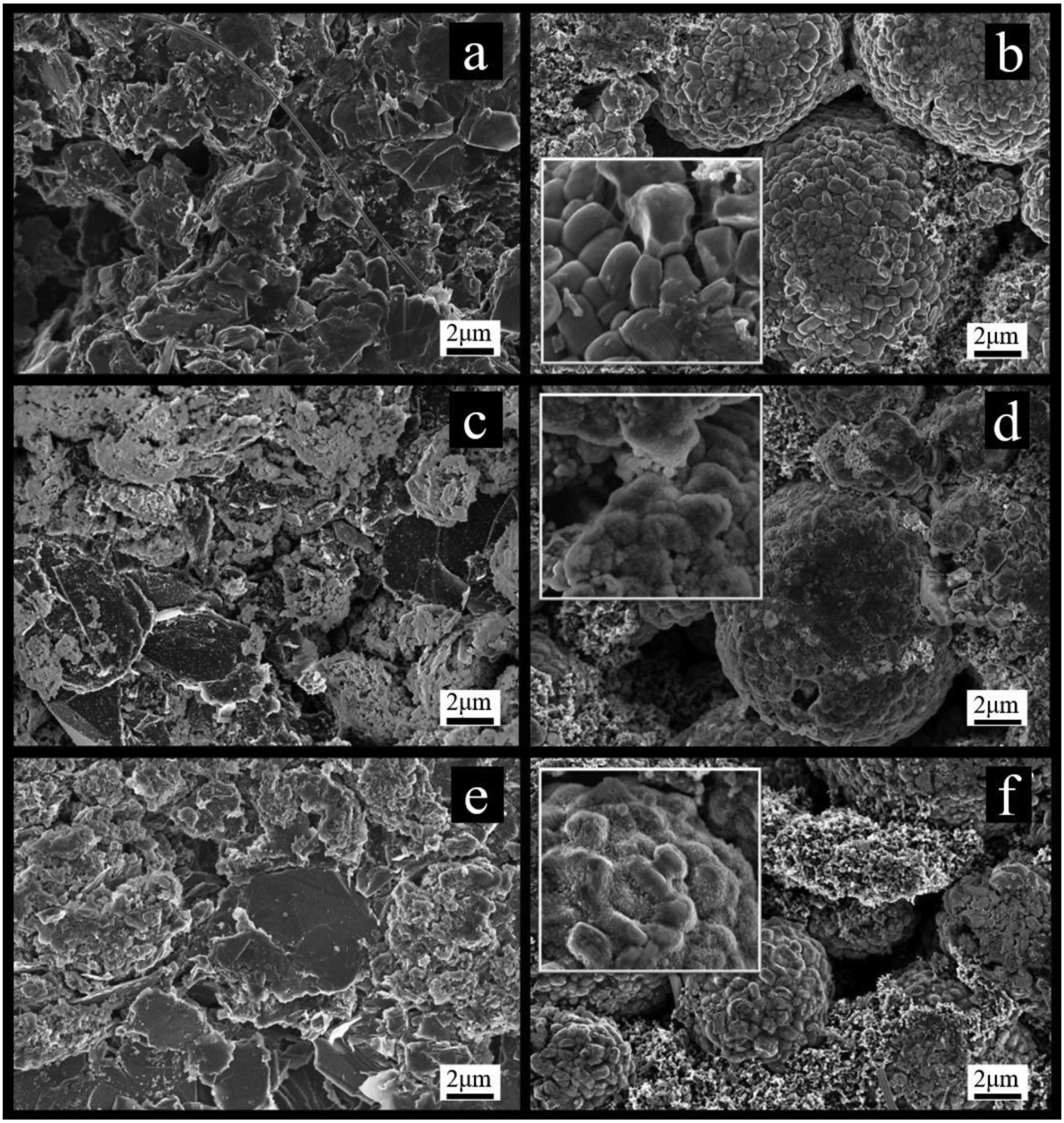

Fig. 6. SEM images of (a) Pristine SiC_x electrode, (b) Pristine NMC-811 electrode, (c) non-prelithiated SiC_x electrode after 300 cycles, (d) NMC-811 electrode cycled in the reference cell, (e) prelithiated SiC_x electrode after 300 cycles, and (e) NMC-811 electrode cycled in the prelithiated cell (Magnification: 5kx, EHT: 3 kV, Signal A: InLens).

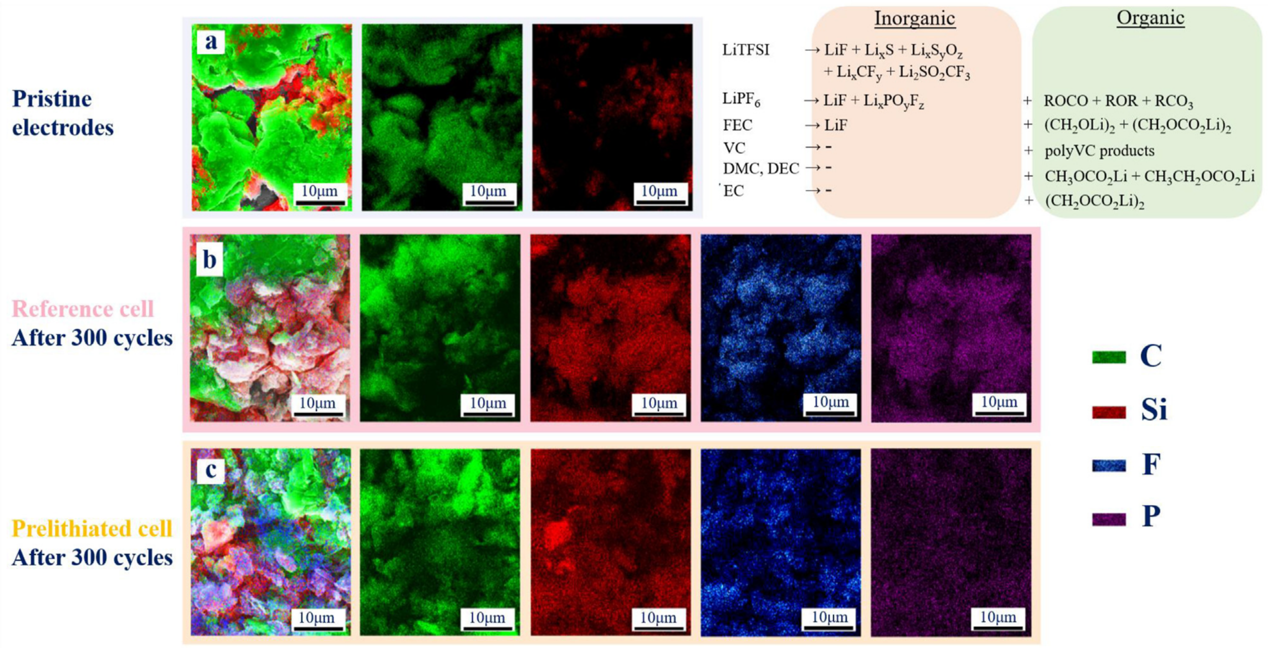

Fig. 7. Elemental composition via EDX of (a) pristine SiC_x electrode (before cycling), (b) non-prelithiated SiC_x electrode after 300 cycles, and c) prelithiated SiC_x electrode after 300 cycles. Green color shows carbon element on the surface while red, blue and violet colors represent silicon, fluorine, and phosphorus, respectively (For interpretation of the references to color in this figure legend, the reader is referred to the Web version of this article).

rest in terms of ICE and cycle life. During this rest time, a FEC-derived SEI grows and seems favorable for achieving final passivation during the formation cycle (with a high ICE and protective SEI for further cycling), whereas after one week, extensive reactivity and possibly disappearance of Li metal and redissolution of SEI compounds (as potential would then increase) would result in too high reactivity and a dramatic impedance increase.

3.4.2. *XPS analysis*

XPS analysis was done after 300 cycles for the NMC-811 and SiC_x electrodes cycled in the reference and prelithiated cells to investigate the CEI and SEI compositions. The elemental composition of the Li, F, P, C, O, Si, and N on the top layers of the SEI and CEI is shown in Table 2. C1s data that includes graphite and organic components hydrocarbon (C1 ~285 eV) [52], polyether carbon (C2 and C3: 286 eV–287.2 eV) [52], and semi-carbonates (C5 ~290 eV) [53] are not discussed in detail as overlapping bands make it difficult to evaluate the data. The percentage of detected S atoms was low ($\leq$0.5%) for all electrodes, especially in the prelithiated cell; thus, it is concluded that the contribution of LiTFSI reduction products in the passivation films, as Li_2S or Li_2SO_4, was scarce for both the reference and the prelithiated cells. The elemental distribution of the top layer (uppermost 5–10 nm) is shown in Fig. 8 for all investigated electrodes. At first glance, the main difference is the higher percentage of Li1s and the lower percentage of P2p for the prelithiated SiC_x electrode, as F1s, O1s, and C1s% are similar for the two SiC_x electrodes. Since multiple SEI and CEI components contain F, Li, C, and O elements, each peak was fitted (Figs. S8–S11) in order to distinguish the contribution of the different chemical species in the SEIs and CEIs. The assignment of the peaks is shown in Table 3.

3.4.2.1. *SiC_x electrode.*

The main conductive salt (1 M) $LiPF_6$ is the only P source in the electrolyte, which mostly contributed the SEI films on both electrodes as LiF since the P2p ratio was low for both SiC_x electrodes. The fluorinated phosphates ($Li_xPF_yO_z$) (P2) are rather low for both electrodes but 8% higher than the polyphosphates in the SEI films on the prelithiated SiC_x. Furthermore, Li_3PO_4 (Li2) was detected on the top surface of the SEI film in the prelithiated cells, while it is not present in the SEI of the reference

Table 2
Elemental composition (%*) of the top layer (5–10 nm) of NMC-811 and SiC_x electrodes cycled in reference and prelithiated cells. (300 cycles, $T_{cycling}$: 20 °C, *concentrations of all detected elements were normalized to 100 atomic %).

Elemental composition (%) (5–10 nm)	C	N	S	O	F		P		Li	
					F1	F2	P1	P2	Li1	Li2
Reference SiC_x	35.8 ± 3.2	0.5 ± 0	0.4 ± 0.2	23.0% ± 2.2	21.6 ± 3.1		5.0 ± 0.5		13.7 ± 2.2	
					82.5% (±1.4)	17.5% (±1.4)	55.1% (±8.5)	44.9% (±8.5)	100%	0%
Prelithiated SiC_x	42.8 ± 1.4	0.05 ± 0.07	0.7 ± 0.1	25.4 ± 0.1	14.2 ± 1.1		2.4 ± 0.1		14.6 ± 0.5	
					64.1% (±2.0)	35.9% (±2.0)	46.9% (±5.2)	53.1% (±5.2)	94.0% (±2.5)	6.0% (±2.5)
NMC-811 Cycled in reference cell	38.8 ± 2.4	0.45 ± 0.07	0.1 ± 0	21.8 ± 0.1	23.4 ± 1.8		3.1 ± 0.1		12.2 ± 0.6	
					83.1% (±5.6)	16.9% (±5.6)	39.7% (±2.0)	60.3% (±2.0)	19.2% (±1.8)	80.8% (±1.8)
NMC-811 Cycled in prelithiated cell	44.7 ± 1.0	0.1 ± 0	0.2 ± 0	23.6 ± 0.6	23.6 ± 0.6		3.2 ± 0.5		4.7 ± 0.6	
					99.4% (±0.2)	0.6% (±0.2)	47.6% (±1.5)	52.4% (±1.5)	33.3% (±6.6)	66.7% (±6.6)

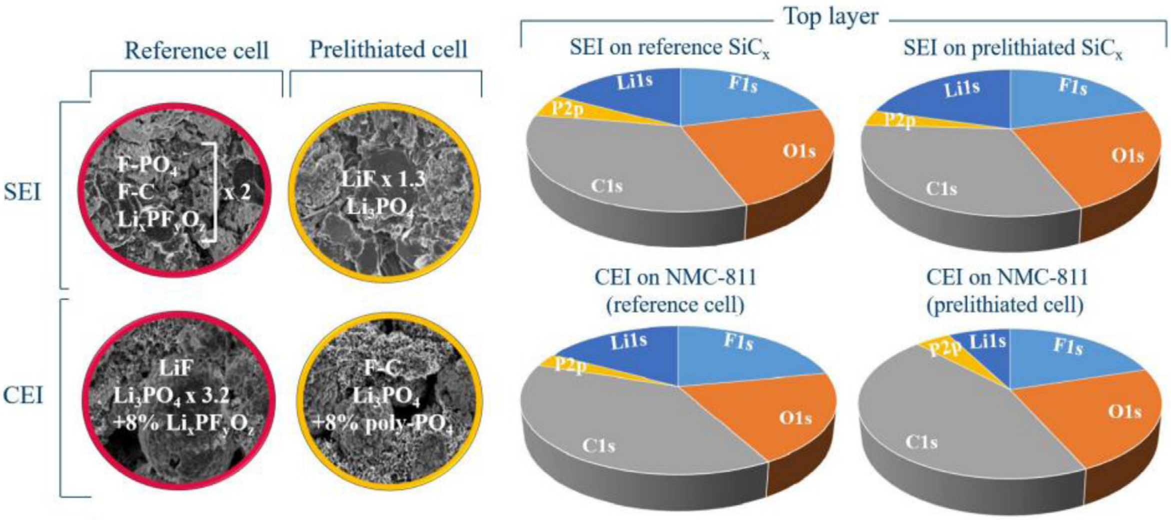

Fig. 8. Elemental distribution of top layers of SEI and CEI in reference and prelithiated cells after 300 cycles ($T_{cycling}$: 20 °C).

SiC_x electrode. The main difference in the SEI films is the F1s contribution. LiF (Li1) is 1.3 times higher for the prelithiated SiC_x electrode compared with the reference cell, which is coherent with the EDX results. Meanwhile, the F1 signal related to fluorinated carbons $Li_xPO_yF_z$, $Li_xPF_yO_z$ and Li_xPF_y for the reference SiC_x is twice that of the prelithiated SiC_x electrode. It should be noted that these P-containing compounds in the SEI form are a result of the reaction of $LiPF_6$ with electrolyte solvents such as EC, and as shown by Lucht et al. they are accompanied by acidic species such as difluorophosphoric acid (F_2PO_2H) [58]. Furthermore, they showed that the formation of such acidic products severely damages the passivation film on the anode as they react with SEI components such as lithium ethylene dicarbonate (LEDC), leading to capacity decay during cycling [58,59]. Thus, having less of these components hints to the superiority of the SEI formed on the prelithiated SiC_x electrode.

3.4.2.2. NMC-811 electrodes. The content of C1s is 6% higher for the NMC-811 electrode cycled against the prelithiated SiC_x electrode. It suggests a CEI with fewer inorganic components. Furthermore, the percentages of F1s and P2p are similar for both NMC-811 electrodes. However, for the reference NMC-811, 16.9% of the F1s signal is related to LiF, whereas almost no LiF was detected for the CEI in the prelithiated cell. The Li1 and Li2 fractions confirm that the reference NMC-811 electrode contains more LiF (Li1) and Li_3PO_4 (Li2, 3.2 times) in the CEI. Additionally, since there are 8% fewer polyphosphates and 8% more $Li_xPF_yO_z$, it indicates that the reference CEI is richer in inorganic components. A CEI layer richer in resistive inorganic components could contribute to the faster capacity decay of the reference cells throughout long-term cycling.

3.4.2.3. Depth profiling. The change of the elemental distribution was measured by XPS for all electrodes from the top surface to 96 nm depth by sputtering depth profiling (ca. 16 nm per sputtering step), and the results are shown in Fig. 9. For both reference and prelithiated SiC_x electrodes, F1s and Li1s signals increase notably after the first ablation (~-16 nm), while O1s, C1s, and P2p percentages decrease. This indicates an increase in inorganic components such as LiF, Li_3PO_4, and $Li_xPO_yF_z$ near the electrode surface. I The increase in F1s and Li1s signals is more marked for the reference SiC_x electrode, accompanied by a sharper decrease in carbon signal (C1s) compared to the prelithiated cell. It seems to indicate that the SEI is more inorganic near the surface of the reference electrode. It is coherent that the more organic SEI of the prelithiated SiC_x electrode is more flexible, less brittle, and thereby more protective.

For the reference NMC-811 electrode, the trend of the change in elemental composition after first etching (16 nm) is similar to that of the SiC_x electrodes, showing an increased fraction of inorganic components with etching. The main difference for the NMC-811 electrode cycled against the prelithiated SiC_x is a much lower F1s signal compared to the reference cell, indicating a lower percentage

Table 3
Assigned organic and inorganic components of the passivation films on NMC-811 and SiC_x electrodes after 300 cycles.

F1s	F1 (~687.6 eV)		F2 (~685.5 eV)	
	Fluorine-carbon (~687 eV) [54]		LiF (685 eV) [43]	
	$Li_xPO_yF_z$ (~687.2 eV) [55]			
	$Li_xPF_yO_z$ + Li_xPF_y (~688.2 eV) [43]			
Li1s	Li1 (~55.8 eV)		Li2 (~54.5 eV)	
	LiF (~55.9 eV) [53]		Li_3PO_4 (~55.4 eV) [53]	
P2p	P1 (~134.8 eV)		P2 (~136.7 eV)	
	Poly-phosphate P—O—P (~134 eV) [55,56]		$Li_xPF_yO_z$ (~136 eV) [43]	
O1s	**O1 (~528 eV)**	**O2 (~532.4 eV)**	**O3 (~533.0 eV)**	**O4 (~534.4 eV)**
	Li_2O (~528.8 eV) [55]	Poly-ether (~531.3 eV) [53]	Oxyfluorinated carbon (~533.0 eV) [54]	Epoxides (~534.4 eV) [57]
			C—O species (~533.0 eV) [55]	
			Hydroxyl groups (~533.2 eV) [57]	
C1s	**C1—C5 (285 eV − 291 eV)**			
	Graphite/hydrocarbon (~284.8 eV) [52], poly-ether carbon (~286.5 eV) [52], semicarbonates (R-CH_2OCO_2Li from $LiPF_6$) [52], Li_2CO_3 [53]			

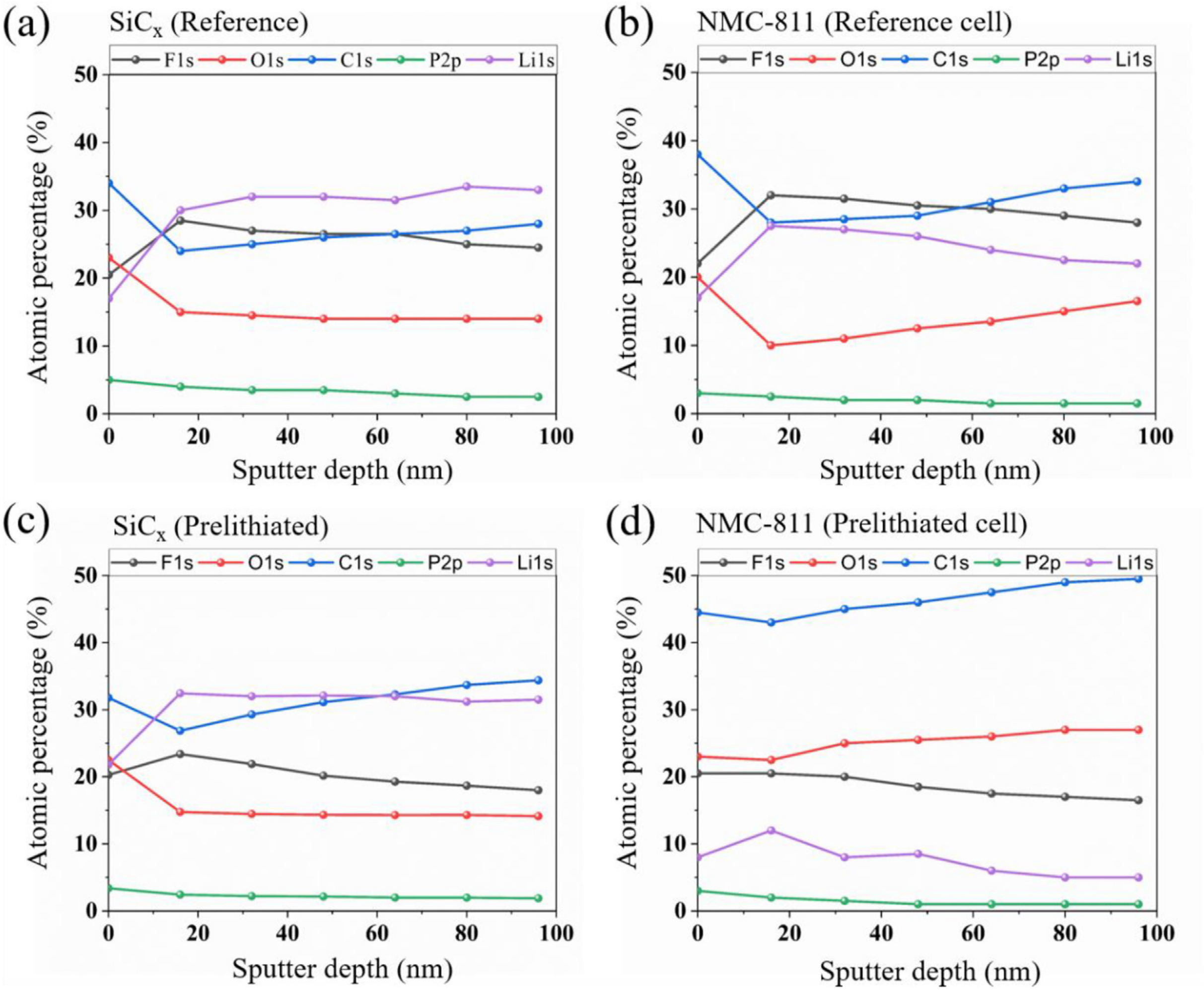

Fig. 9. Depth profiling of (a) non-prelithiated SiC$_x$ electrode and (b) NMC-811 electrode cycled in reference cell, (c) prelithiated SiC$_x$ electrode and (c) NMC-811 electrode cycled in the prelithiated cell. (300 cycles, ablation rate: 16 nm per etching, T$_{measurement}$: 23 °C).

of inorganic components such as LiF, Li$_x$PF$_y$, and Li$_x$PO$_y$F$_z$. The gradual decrease of the F1s signal is continuous throughout the etching process. It is thus likely that the prelithiation has generated more organic compounds that have been deposited onto both electrodes and helped form more robust SEI and CEI.

4. Conclusion

For prelithiated SiC$_x$ electrodes, EIS showed that the SEI continuously grows during storage time and that its resistance increases very significantly after 7 days of storage. This corresponds to the disappearance of Li metal, observed by NMR, that is inserted into the anode and consumed by the SEI formation. Once the lithium disappears, after 7 days, the anode self-discharge leads to less favorable growth of SEI, which increases the cell resistance and decreases its performance in terms of cycle life and ICE. Thus, the building of SEI for 7 days and the total disappearance of Li metal are optimal for cell performance. GITT showed that Li diffusion inside the prelithiated SiC$_x$ electrode is slower compared to the reference SiC$_x$ electrode due to thicker SEI formation, but fully lithiated species such as LiC$_6$ and Li$_{15}$Si$_4$ are then formed in the prelithiated SiC$_x$ electrode during the first charge. In addition to providing a Li reservoir and shifting the potential range at which the anode is cycled within a lower potential range, differences in both SEI and CEI compositions have been observed by EDX and XPS, which probably contribute to the higher cell performance of the prelithiated cells. In particular, a SEI layer richer in fluorinated phosphates is formed on the non-prelithiated SiC$_x$ electrode, whereas the SEI on the prelithiated SiC$_x$ electrode is richer in inorganic components such as LiF and Li$_3$PO$_4$. It is also shown that prelithiation of the negative electrode affected the passivation film on the positive electrode, as LiF was not observed and Li$_3$PO$_4$ was much less on the NMC-811 electrode cycled against the prelithiated SiC$_x$ electrode.

Declaration of competing interest

The authors declare the following financial interests/personal relationships which may be considered as potential competing interests:

Elie Paillard reports financial support was provided by European Commission. Ekin Esen reports financial support was provided by European Commission.

Acknowledgment

The research reported is part of the 'SPIDER' project funded by the European Union's Horizon 2020 research and innovation program under grant agreement n° 814389.

Appendix A. Supplementary data

Supplementary data to this article can be found online at https://doi.org/10.1016/j.mtchem.2023.101587.

References

[1] R. Schmuch, R. Wagner, G. Hörpel, Performance and cost of materials for lithium-based rechargeable automotive batteries, Nat. Energy 3 (2010) 267–278, https://doi.org/10.1038/s41560-018-0107-2.

[2] Vehicle Technologies Office Annual Merit Review 2017 Report 2017 13.12.2021]; Available from: https://www1.eere.energy.gov/vehiclesandfuels/downloads/VTO_2020_APR_Batteries_compliant_.pdf.

[3] S. Goutam, N. Omar, P. Van Den Bossche, J. Van Mierlo, Review of nanotechnology for anode materials in batteries, Emerg. Nanotechnol. Recharg. Energy Stor. Syst. (2017) 45–82, https://doi.org/10.1016/B978-0-323-42977-1.00002-9.

[4] B. Bulut Kopuklu, A. Gomez-Martin, M. Winter, T. Placke, R. Schmuch, S. Alkan Gursel, A. Yurum, Improved lithium-ion transport within the $LiNi_{0.8}Co_{0.15}Al_{0.05}O_2$ secondary cathode particles through a template-assisted synthesis route, ACS Sustain. Chem. Eng. 9 (2021) 12560–12574, https://doi.org/10.1021/acssuschemeng.1c03179.

[5] K. Märker, P.J. Reeves, X. Chao, K.J. Griffith, C.P. Grey, Evolution of structure and lithium dynamics in $LiNi_{0.8}Mn_{0.1}Co_{0.1}O_2$ (NMC811) cathodes during electrochemical cycling, Chem. Mater. 31 (2019) 2545–2554, https://doi.org/10.1021/acs.chemmater.9b00140.

[6] B. Boukamp, G. Lesh, R. Huggins, All-solid lithium electrodes with mixed-conductor matrix, J. Electrochem. Soc. 128 (1981) 725, https://doi.org/10.1149/1.2127495.

[7] D.Y. Yu, M. Zhou, H. Hoster, Suppressing vertical displacement of lithiated silicon particles in high volumetric capacity battery electrodes, ChemElectroChem 2 (2015) 1090–1095, https://doi.org/10.1002/celc.201500133.

[8] V. Müller, R.G. Scurtu, K. Richter, T. Waldmann, M. Memm, M.A. Danzer, M. Wohlfahrt-Mehrens, Effects of mechanical compression on the aging and the expansion behavior of Si/C-composite| NMC811 in different lithium-ion battery cell formats, J. Electrochem. Soc. 166 (2019) A3796, https://doi.org/10.1149/2.1121915jes.

[9] M. Wetjen, D. Pritzl, R. Jung, S. Solchenbach, R. Ghadimi, H.A. Gasteiger, Differentiating the degradation phenomena in silicon-graphite electrodes for lithium-ion batteries, J. Electrochem. Soc. 164 (2017), A2840, https://doi.org/10.1149/2.1921712jes.

[10] T. Yoon, C.C. Nguyen, D.M. Seo, B.L. Lucht, Capacity fading mechanisms of silicon nanoparticle negative electrodes for lithium ion batteries, J. Electrochem. Soc. 162 (2015) A2325, https://doi.org/10.1149/2.0731512jes.

[11] M.W. Forney, M.J. Ganter, J.W. Staub, R.D. Ridgley, B.J. Landi, Prelithiation of silicon–carbon nanotube anodes for lithium ion batteries by stabilized lithium metal powder (SLMP), Nano Lett. 13 (2013) 4158–4163, https://doi.org/10.1021/nl401776d.

[12] S.-K. Jeong, M. Inaba, R. Mogi, Y. Iriyama, T. Abe, Z. Ogumi, Surface film formation on a graphite negative electrode in lithium-ion batteries: atomic force microscopy study on the effects of film-forming additives in propylene carbonate solutions, Langmuir 17 (2001) 8281–8286, https://doi.org/10.1021/la015553h.

[13] Y. Okuno, K. Ushirogata, K. Sodeyama, Y. Tateyama, Decomposition of the fluoroethylene carbonate additive and the glue effect of lithium fluoride products for the solid electrolyte interphase: an ab initio study, Phys. Chem. Chem. Phys. 18 (2016) 8643–8653, https://doi.org/10.1039/C5CP07583A.

[14] S.R. Sivakkumar, A. Pandolfo, Evaluation of lithium-ion capacitors assembled with pre-lithiated graphite anode and activated carbon cathode, Electrochim. Acta 65 (2012) 280–287, https://doi.org/10.1016/j.electacta.2012.01.076.

[15] P. Jeżowski, O. Crosnier, E. Deunf, P. Poizot, F. Béguin, T. Brousse, Safe and recyclable lithium-ion capacitors using sacrificial organic lithium salt, Nat. Mater. 17 (2018) 167–173, https://doi.org/10.1038/nmat5029.

[16] M. Arnaiz, D. Shanmukaraj, D. Carriazo, D. Bhattacharjya, A. Villaverde, M. Armand, J. Ajuria, A transversal low-cost pre-metallation strategy enabling ultrafast and stable metal ion capacitor technologies, Energy Environ. Sci. 13 (2020) 2441–2449, https://doi.org/10.1039/D0EE00351D.

[17] H. Sun, X. He, J. Ren, J. Li, C. Jiang, C. Wan, Hard carbon/lithium composite anode materials for Li-ion batteries, Electrochim. Acta 52 (2007) 4312–4316, https://doi.org/10.1016/j.electacta.2006.12.012.

[18] N. Liu, L. Hu, M.T. McDowell, A. Jackson, Y. Cui, Prelithiated silicon nanowires as an anode for lithium ion batteries, ACS Nano 5 (2011) 6487–6493, https://doi.org/10.1021/nn2017167.

[19] C.R. Jarvis, M.J. Lain, M.V. Yakovleva, Y. Gao, A prelithiated carbon anode for lithium-ion battery applications, J. Power Sources 162 (2016) 800–802, https://doi.org/10.1016/j.jpowsour.2005.07.051.

[20] H. Zhao, Z. Wang, P. Lu, M. Jiang, F. Shi, X. Song, Z. Zheng, X. Zhou, Y. Fu, G. Abdelbast, V.S. Battaglia, X. Xiao, Z. Liu, K. Zaghib, G. Liu, Toward practical application of functional conductive polymer binder for a high-energy lithium-ion battery design, Nano Lett. 14 (2014) 6704–6710, https://doi.org/10.1021/nl503490h.

[21] D. Shanmukaraj, S. Grugeon, S. Laruelle, G. Douglade, J.M. Tarascon, M. Armand, Sacrificial salts: compensating the initial charge irreversibility in lithium batteries, Electrochem. Commun. 12 (2010) 1344–1347, https://doi.org/10.1016/j.elecom.2010.07.016.

[22] P. Jeżowski, K. Fic, O. Crosnier, T. Brousse, F. Béguin, Lithium rhenium (vii) oxide as a novel material for graphite pre-lithiation in high performance lithium-ion capacitors, J. Mater. Chem. 4 (2016) 12609–12615, https://doi.org/10.1039/C6TA03810G.

[23] Y. Sun, H.W. Lee, G. Zheng, Z. Seh, J. Sun, Y. Li, Y. Cui, In situ chemical synthesis of lithium fluoride/metal nanocomposite for high capacity prelithiation of cathodes, Nano Lett. 16 (2016) 1497–1501, https://doi.org/10.1021/acs.nanolett.5b05228.

[24] Z. Wang, Y. Fu, Z. Zhang, S. Yuan, K. Amine, V. Battaglia, G. Liu, Application of stabilized lithium metal powder (SLMP®) in graphite anode–a high efficient prelithiation method for lithium-ion batteries, J. Power Sources 260 (2014) 57–61, https://doi.org/10.1016/j.jpowsour.2014.02.112.

[25] A. Rezqita, A.R. Kathribail, J. Kahr, M. Jahn, Analysis of degradation of Si/carbon|| LiNi0.5Mn0.3Co0.2O2 full cells: effect of prelithiation, J. Electrochem. Soc. 166 (2019) A5483, https://doi.org/10.1149/2.0671903jes.

[26] J. Bisquert, Theory of the impedance of electron diffusion and recombination in a thin layer, J. Phys. Chem. B 106 (2) (2002) 325–333.

[27] E. Allcorn, S.O. Kim, A. Manthiram, Lithium diffusivity in antimony-based intermetallic and FeSb–TiC composite anodes as measured by GITT, Phys. Chem. Chem. Phys. 17 (2015) 28837–28843, https://doi.org/10.1039/C5CP04023J.

[28] W. Choi, H.C. Shin, J. Kim, J.Y. Choi, W.S. Yoon, Modeling and applications of electrochemical impedance spectroscopy (EIS) for lithium-ion batteries, J. Electrochem. Sci. Technol. 11 (2020) 1–13, https://doi.org/10.33961/jecst.2019.00528.

[29] F. Holtstiege, P. Bärmann, R. Nölle, M. Winter, T. Placke, Pre-lithiation strategies for rechargeable energy storage technologies: concepts, promises and challenges, Batteries 4 (2018) 4, https://doi.org/10.3390/batteries4010004.

[30] M.A. Danzer, Generalized distribution of relaxation times analysis for the characterization of impedance spectra, Batteries 5 (2019) 53, https://doi.org/10.3390/batteries5030053.

[31] C.C. Nguyen, T. Yoon, D.M. Seo, P. Guduru, B.L. Lucht, Systematic investigation of binders for silicon anodes: interactions of binder with silicon particles and electrolytes and effects of binders on solid electrolyte interphase formation, ACS Appl. Mater. Interfaces 8 (2016) 12211–12220, https://doi.org/10.1021/acsami.6b03357.

[32] H. Bryngelsson, M. Stjerndahl, T. Gustafsson, K. Edström, How dynamic is the SEI? J. Power Sources 174 (2007) 970–975, https://doi.org/10.1016/j.jpowsour.2007.06.050.

[33] O. Pecher, J. Carretero-González, K.J. Griffith, C.P. Grey, Materials' methods: NMR in battery research, Chem. Mater. 29 (2017) 213–242, https://doi.org/10.1021/acs.chemmater.6b03183.

[34] A. Shellikeri, V.G. Watson, D.L. Adams, E.E. Kalu, J.A. Read, T.R. Jow, J.P. Zheng, Pre-lithiation of carbon anodes using different lithium-sources, ECS Trans. 77 (2017) 293, https://doi.org/10.1149/07711.0293ecst.

[35] P. Bärmann, M. Mohrhardt, J. E Frerichs, M. Helling, A. Kolesnikov, S. Klabunde, S. Nowak, M.R. Hansen, M. Winter, T. Placke, Mechanistic insights into the pre-lithiation of silicon/graphite negative electrodes in "dry state" and after electrolyte addition using passivated lithium metal powder, Adv. Energy Mater. 11 (2021), 2100925, https://doi.org/10.1002/aenm.202100925.

[36] K.P. Yao, J.S. Okasinski, K. Kalaga, J.D. Almer, D.P. Abraham, Operando quantification of (de) lithiation behavior of silicon–graphite blended electrodes for lithium-ion batteries, Adv. Energy Mater. 9 (2019), 1803380, https://doi.org/10.1002/aenm.201803380.

[37] M.T. McDowell, S.W. Lee, W.D. Nix, Y. Cui, 25th anniversary article: understanding the lithiation of silicon and other alloying anodes for lithium-ion batteries, Adv. Mater. 25 (2013) 4966–4985, https://doi.org/10.1002/adma.201301795.

[38] P. Yu, B.N. Popov, J.A. Ritter, R.E. White, Determination of the lithium ion diffusion coefficient in graphite, J. Electrochem. Soc. 146 (1999) 8, https://doi.org/10.1149/1.1391556.

[39] P. Lory, B. Mathieu, S. Genies, Y. Reynier, A. Boulineau, W. Hong, M. Chandesris, Probing silicon lithiation in silicon-carbon blended anodes with a multi-scale porous electrode model, J. Electrochem. Soc. 167 (2020), 120506, https://doi.org/10.1149/1945-7111/abaa69.

[40] J. Harlow, S.L. Glazier, J. Li, J.R. Dahn, Use of asymmetric average charge-and average discharge-voltages as an indicator of the onset of unwanted lithium deposition in lithium-ion cells, J. Electrochem. Soc. 165 (2018), A3595, https://doi.org/10.1149/2.0011816jes.

[41] S. Benning, C. Chen, R.A. Eichel, P.H. Notten, F. Hausen, Direct observation of SEI formation and lithiation in thin-film silicon electrodes via in Situ electrochemical atomic force microscopy, ACS Appl. Energy Mater. 2 (2019) 6761–6767, https://doi.org/10.1021/acsaem.9b01222.

[42] J.L. Schaefer, Y. Lu, S.S. Moganty, P. Agarwal, N. Jayaprakash, L.A. Archer, Electrolytes for high-energy lithium batteries, Appl. Nanosci. 2 (2012) 91–109, https://doi.org/10.1007/s13204-011-0044-x.

[43] B.S. Parimalam, B.L. Lucht, Reduction reactions of electrolyte salts for lithium ion batteries: LiPF6, LiBF4, LiDFOB, LiBOB, and LiTFSI, J. Electrochem. Soc. 165 (2018), A251, https://doi.org/10.1149/2.0901802jess.

[44] S.A. Delp, O. Borodin, M. Olguin, C.G. Eisner, J.L. Allen, T.R. Jow, Importance of reduction and oxidation stability of high voltage electrolytes and additives, Electrochim. Acta 209 (2016) 498–510, https://doi.org/10.1016/j.electacta.2016.05.100.

[45] S.P. Nadimpalli, V.A. Sethuraman, S. Dalavi, B. Lucht, M.J. Chon, V.B. Shenoy, P.R. Guduru, Quantifying capacity loss due to solid-electrolyte-interphase layer formation on silicon negative electrodes in lithium-ion batteries, J. Power Sources 215 (2012) 145–151, https://doi.org/10.1016/j.jpowsour.2012.05.004.
[46] K.W. Schroder, H. Celio, L.J. Webb, K.J. Stevenson, Examining solid electrolyte interphase formation on crystalline silicon electrodes: influence of electrochemical preparation and ambient exposure conditions, J. Phys. Chem. C 116 (2012) 19737–19747, https://doi.org/10.1021/jp307372m.
[47] M. Sina, H. Shobukawa, C. Alexander, V. Manichev, L. Feldman, T. Gustafsson, K.J. Stevenson, Y.S. Meng, Direct visualization of the solid electrolyte interphase and its effects on silicon electrochemical performance, Adv. Mater. Interfac. 3 (2016), 1600438, https://doi.org/10.1002/admi.201600438.
[48] Y. Zhang, D. Krishnamurthy, V. Viswanathan, Engineering solid electrolyte interphase composition by assessing decomposition pathways of fluorinated organic solvents in Lithium metal batteries, J. Electrochem. Soc. 167 (2020), 070554, https://doi.org/10.1149/1945-7111/ab836b.
[49] C. Zhang, Q. Lan, Y. Liu, J. Wu, H. Shao, H. Zhan, Y. Yang, A dual-layered artificial solid electrolyte interphase formed by controlled electrochemical reduction of LiTFSI/DME-LiNO3 for dendrite-free lithium metal anode, Electrochim. Acta 306 (2019) 407–419, https://doi.org/10.1016/j.electacta.2019.03.162.
[50] N. Takenaka, H. Sakai, Y. Suzuki, P. Uppula, M. A, Nagaoka computational chemical insight into microscopic additive effect on solid electrolyte interphase film formation in sodium-ion batteries: suppression of unstable film growth by intact fluoroethylene carbonate, J. Phys. Chem. C 119 (2015) 18046–18055, https://doi.org/10.1021/acs.jpcc.5b04206.
[51] C. Xu, F. Lindgren, B. Philippe, M. Gorgoi, F. Björefors, K. Edstrom, T. Gustafsson, Improved performance of the silicon anode for Li-ion batteries: understanding the surface modification mechanism of fluoroethylene carbonate as an effective electrolyte additive, Chem. Mater. 27 (2015) 2591–2599, https://doi.org/10.1021/acs.chemmater.5b00339.
[52] K. Xu, U. Lee, S. Zhang, M. Wood, T.R. Jow, Chemical analysis of graphite/electrolyte interface formed in LiBOB-based electrolytes, Electrochem. Solid State Lett. 6 (2013), A144, https://doi.org/10.1149/1.1576049.
[53] K. Xu, G.V. Zhuang, J.L. Allen, U. Lee, S.S. Zhang, P.N. Ross Jr., T.R. Jow, Syntheses and characterization of lithium alkyl mono-and dicarbonates as components of surface films in Li-ion batteries, J. Phys. Chem. B 110 (2006) 7708–7719, https://doi.org/10.1021/jp0601522.
[54] S.-M. Yun, J.W. Kim, M.J. Jung, Y.C. Nho, P.H. Kang, Y.S. Lee, An XPS study of oxyfluorinated multiwalled carbon nano tubes, Carbon Lett. 8 (2007) 292–298, https://doi.org/10.5714/CL.2007.8.4.292.
[55] M.S. Milien, U. Tottempudi, M. Son, M. Ue, B.L. Lucht, Development of lithium dimethyl phosphate as an electrolyte additive for lithium ion batteries, J. Electrochem. Soc. 163 (2016), A1369, https://doi.org/10.1149/2.1131607jes.
[56] K.S. Siow, L. Britcher, S. Kumar, H.J. Griesser, Deposition and XPS and FTIR analysis of plasma polymer coatings containing phosphorus, Plasma Process. Polym. 11 (2014) 133–141, https://doi.org/10.1002/ppap.201300115.
[57] Y.C.G. Kwan, G.M. Ng, C.H.A. Huan, Identification of functional groups and determination of carboxyl formation temperature in graphene oxide using the XPS O1s spectrum, Thin Solid Films 590 (2015) 40–48, https://doi.org/10.1016/j.tsf.2015.07.051.
[58] C. Jayawardana, N. Rodrigo, B. Parimalam, B.L. Lucht, Role of electrolyte oxidation and difluorophosphoric acid generation in crossover and capacity fade in lithium ion batteries, ACS Energy Lett. 6 (2021) 3788–3792, https://doi.org/10.1021/acsenergylett.1c01657.
[59] S.K. Heiskanen, N. Laszczynski, B.L. Lucht, Perspective—surface reactions of electrolyte with $LiNi_xCo_yMn_zO_2$ cathodes for lithium ion batteries, J. Electrochem. Soc. 167 (2020), 100519, https://doi.org/10.1149/1945-7111/ab981c.